Characterization for vision science applications of a bimorph deformable mirror using Phase-Shifting Interferometry

David A. Horsley[a], Hyunkyu Park[a], Sophie P. Laut[b], John S. Werner[b]

[a]Dept. of Mechanical and Aeronautical Engineering, University of California, One Shields Avenue, Davis, CA 95616, USA;
[b]Dept. of Ophthalmology and Visual Science, UC Davis Medical Center, 4860 Y Street, Suite 2400, Sacramento, CA 95817, USA

ABSTRACT

The wave front corrector is one of the three key elements in adaptive optics, along with the wave front sensor and the control computer. Low cost, compact deformable mirrors are increasingly available. We have tested the AOptix bimorph deformable mirror, originally developed for ultra-high bandwidth laser communication systems, to determine its suitability for vision science applications, where cornea and lens introduce optical aberrations. Measurements of the dynamic response of the mirror to a step input were obtained using a commercial Laser Doppler Vibrometer (LDV). A computer-controlled Twyman-Green interferometer was constructed to allow the surface height of the deformable mirror to be measured using Phase-Shifting Interferometry as a function of various control voltages. A simple open-loop control method was used to compute the control voltages required to generate aberration mode shapes described by the Zernike polynomials. Using this method, the ability of the deformable mirror to generate each mode shape was characterized by measuring the maximum amplitude and RMS error of each Zernike mode shape up to the fifth radial order. The maximum deformation amplitude was found to diminish with the square of the radial order of the Zernike mode, with a measured deformation of 8 microns and 1.5 microns achieved at the second-order and fifth-order Zernike modes, respectively. This deformation amplitude appears to be sufficient to allow the mirror to correct for aberrations up to the fifth order in the human eye.

Keywords: deformable mirrors, interferometry, adaptive optics systems, vision science

1. INTRODUCTION

The application of adaptive optics (AO) to the field of vision science [1] has continued to increase since its first implementation by Liang in the 90's [2]. Recent applications include super-resolution fundus imagers [3-8], as well as the integration of AO with ophthalmic instruments like the Scanning Laser Ophthalmoscope (SLO) [9, 10] and the Optical Coherence Tomograph (OCT) [11], where it offers new capabilities for the early detection and diagnosis of retinal diseases. In parallel with the medical applications of AO for vision science, there has also been a great interest in the psychophysics of supernormal vision [12-14]. The major obstacle for the transfer of this technology from current research laboratory prototypes into commercial systems for general clinical use is the large size and prohibitive cost of the phase corrector.

The various phase-correctors used in AO systems for vision science were recently reviewed by Doble and Williams [15]. These include the liquid-crystal (LC) spatial light modulator (SLM) and the deformable mirror (DM). Table 1 contains a short summary of the devices which have been used in vision science applications to date. Although LC SLM's have the advantage of high spatial resolution, they have proven complex to calibrate and have the disadvantage of dependence on the wavelength and polarization of the incident light [16, 17]. For this reason, most researchers have built their AO systems around a DM. The most common DM's are continuous face-sheet mirrors such as those produced by Xinetics (Devens, MA) [18]. The Xinetics DM consists of a thin mirror surface which is bonded to an array of columnar actuators which push and pull the mirror surface in a piston-like fashion. Because these devices were originally designed for large-aperture astronomical applications, they require the 7 mm human pupil to be magnified by

10–15×, resulting in a very large instrument size. These DM's have proven very reliable and versatile, but they are costly (around $1000 per actuator), and require high-voltage electronics that are presently bulky and inefficient.

Table 1: Summary of Phase-Correctors Previously Used in Vision Science Applications

Manufacturer	Type	Diameter [mm]	# Actuators	Voltage	Stroke [μm]	Ref.
Hamamatsu	LC-SLM	20	480x480	5	0.8 @ 820 nm	[19]
Xinetics	DM	75	97	100	4	[7]
Xinetics	DM	46	37	100	±2	[2, 9]
Cilas	DM	30	13	±400	±6	[3]
OKO Technologies	MEMS DM	15	37	255	6	[20], [21]
Boston Micromachines	MEMS DM	3.3	12x12	220	±1	[22]

To address the failings of current DM technology, new research has focused on using Micro Electro-Mechanical Systems (MEMS) technology to develop a low-cost DM. To date, the only MEMS DM's that have been used in vision science systems are electrostatically-actuated thin-film devices [23, 24]. In these devices, the deformable mirror surface is composed of a film of material, such as polycrystalline silicon or silicon nitride, which is suspended above a fixed array of control electrodes. The mirror surface is deformed by applying a high voltage, typically 100V-300V, between the mirror surface and the fixed electrodes, creating an electrostatic attraction between the two surfaces. A major advantage of this approach is that it leverages integrated circuit technology to produce a large number of actuators, and may result in DM's with integrated control electronics for reduced power and wiring complexity. For example, Boston Micromachines (Watertown, MA) has developed a MEMS DM with 1024 actuators using this approach. The chief drawbacks are the complexity of the manufacturing process, and the difficulty of achieving large actuator stroke with an electrostatic actuator. To date, the most successful designs are limited to a stroke of approximately 2 μm. Although adequate for astronomical applications, this is a severe restriction for vision science applications, which require correction of over 25 μm of wavefront error. For this reason, this paper explores an alternative MEMS DM based on the bimorph actuation principle. The bimorph DM, produced by AOptix Technologies (Campbell, CA), is composed of two layers of an electromechanically active ceramic which are laminated together. When the mechanical stress in the two layers is equal, the mirror surface is flat. Application of an electric field across either layer results in a stress imbalance between the layers, inducing a curvature in the mirror surface. Bimorph mirrors can generate large actuator stroke and have been successfully utilized in astronomy and telecommunication where atmospheric turbulence results in wavefront errors which are dominated by low order aberrations [25]. The goal of this paper is to determine the suitability of a bimorph mirror for the correction of aberrations for vision science applications.

The maximum order polynomial mode-shape that a DM may reproduce depends on the number of control actuators present on the mirror. In both the Xinetics DM and the Boston Micromachines MEMS DM, the surface height of the DM is directly controlled with individual piston-like actuators. As a result, the maximum deformation amplitude of these mirrors is approximately independent of the spatial frequency of the applied pattern. In contrast, each actuator in the bimorph DM controls the local curvature of the mirror surface, and the maximum deformation of a bimorph diminishes rapidly with increasing spatial frequency. For this reason, although it is clear that the bimorph can correct for low order aberrations of the eye, such as defocus and astigmatism, it is not clear that the bimorph is suitable for correcting higher order aberrations, such as coma and spherical aberration. This paper investigates the ability of the bimorph to replicate aberrations described by Zernike polynomials up to the fifth radial order.

1.1. Characteristics of the AOptix DM

The layout of the AOptix DM is illustrated in plan view and cross-section in Figure 1. The device is composed of two 160 μm thick layers of the electrostrictive ceramic lead magnesium niobate (PMN). Metal electrodes are deposited onto the PMN and the two layers are bonded together with a 25 μm thick layer of conductive adhesive. The metallization on the back face of the DM is patterned to produce 36 electrodes, while the uniform metallization on the front face of the DM produces a single front face electrode. As illustrated in the figure, voltage is applied to the electrodes on the front

and back faces of the DM, with the inner bonded electrodes serving as ground contacts for both layers. The electrodes on the back face of the DM consist of a central pad surrounded by four annular rings of electrodes. The central pad and the electrodes in the two inner rings (channels 1-19) are used to generate local curvature in the mirror surface, while the electrodes in the outer ring (channels 20-35) produce a slope at the edge of the DM. The curvature and slope electrodes are separated by the third annular electrode ring identified as the guard ring. This guard ring may either be held at the same potential as the front face or may be driven independently to produce a 36th actuator channel. The completed mirror assembly is mounted in a housing with manual tip-tilt adjustment and a 10.2 mm clear aperture.

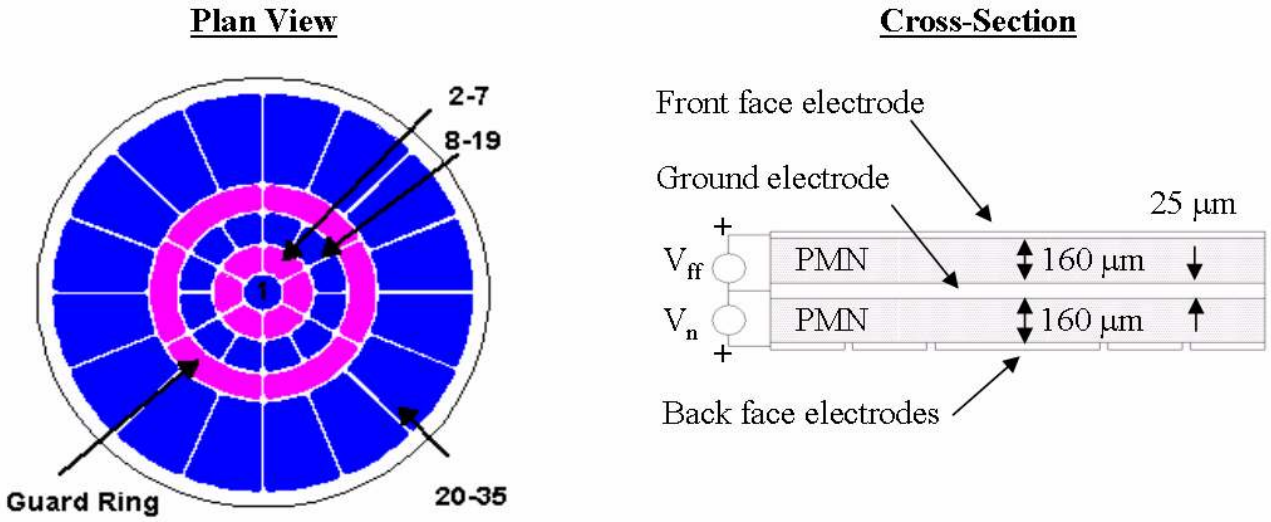

Figure 1: Layout of the AOptix DM: plan view of electrodes (left) and cross-sectional view (right). The numbering of the actuator channels is indicated on the plan view.

PMN is a relaxor ferroelectric material that displays electrostrictive behavior near room temperature [26]. Like piezoelectric materials such as lead zirconium titanate (PZT), electrostrictive materials deform mechanically when an electric field is applied to the material. In contrast to piezoelectrics, in which the direction of deformation reverses with the polarity of the applied field, in electrostriction the deformation direction is independent of the sign of the applied electric field. Although a wide variety of dielectrics possess electrostrictive properties, the effect is particularly large in the relaxor ferroelectrics like PMN. When an electric field is applied to PMN, the material contracts along the transverse axes. Detailed models for the mechanical behavior of deformable mirrors based on the longitudinal extension of PMN are presented in [27] and [28]. In comparison with PZT, PMN has the advantage of greater linearity and lower hysteresis at room temperature. The behavior of PMN and other relaxor ferroelectrics becomes more like that of PZT and other piezoelectrics at temperatures near 273° K, but this temperature dependent behavior is unlikely to be important for clinical AO applications.

In the bimorph structure, voltage applied across the top layer generates a tensile stress in the top layer, causing the bimorph to undergo a concave curvature. Similarly, voltage applied across the bottom layer results in convex curvature. In the absence of any residual stress in the two layers, the DM surface is flat whenever an equal voltage is applied across both the top and bottom layers. Mathematical models for the elastic deformation of bimorph mirrors are described in [29] and [30]. When a uniform electric field is applied across either the top or bottom ceramic layer, the resulting deflection of the mirror surface is approximately parabolic. Because the front face electrode has a capacitance that is more than 36 times greater than the capacitance of the individual back face electrodes, driving this electrode at high frequencies requires considerably greater power and current from the high voltage drive amplifiers. As a result, when employed in a high bandwidth AO system, the front face electrode is normally biased at a constant 100V, and the mirror is flattened by setting the back face electrodes to approximately 100V (plus or minus a small deviation to correct for residual stress produced during mirror fabrication). Local concave or convex surface deformations are then produced by varying the potential on the individual back face electrodes from 0V to 300V.

2. INTERFEROMETRIC TESTING

2.1. Apparatus

The DM is placed in the test path of a Twyman-Green interferometer composed of a polarizing beam splitter (PBS), two quarter-wave plates (QWP), and a flat reference mirror (RM), as illustrated in Figure 2 [31, 32]. The interferometer light source is a fiber-coupled 635-nm laser diode (Hitachi HL6320G), which is expanded and collimated to a 25 mm diameter using two lenses. To ensure uniform illumination of the test and reference mirrors, the optical path is designed so that the beam overfills the second collimating lens. A half-wave plate (HWP) after the collimating optics is used to control the illumination intensity in the test and reference paths of the interferometer in order to compensate for differences in the reflectivity of the reference mirror and the DM. The two quarter-wave plates ensure that the light reflected off the mirrors is directed to a CCD camera (Cohu 6612-1000). A two lens focusing system with a 0.5x magnification forms the image of the DM surface crossed by interference fringes onto the CCD. The CCD images are then digitized using a frame grabber (Matrox Meteor-II), and the resulting interferograms are processed using MATLAB. Measurements of the mirror surface are collected using Hariharan's five-step phase-shifting interferometry technique [33, 34]. Five interferograms are recorded, with each image separated from the previous image by a phase shift of $\pi/2$. The relative phase-shift between the test and reference beams is controlled by moving the reference mirror using a closed-loop piezoelectric stage (Polytec PI P-753.11C). Control voltages are applied to the DM through interface electronics consisting of a 37-channel high-voltage amplifier (HVA) with an RS-422 serial interface.

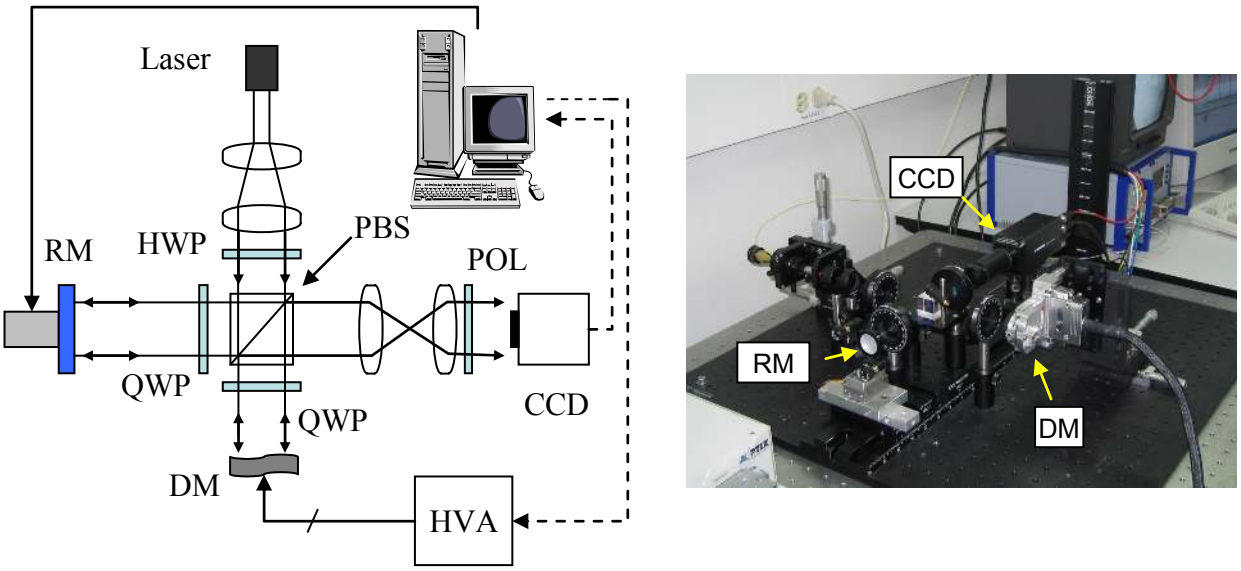

Figure 2: Block diagram of interferometer (left) and photograph of interferometer (right). The DM is visible at the right side of the photograph.

2.2. Calibration of the Interferometer

Initially, the measurement characteristics of the interferometer were characterized by replacing the DM with a ($\lambda/10$) flat mirror. Five sets of five interferograms (25 images in total) were collected as a measure of the repeatability and initial aberrations present in the interferometer setup. The five surface height maps constructed from these measurements are shown in Figure 3. The peak-to-valley surface height was 121 nm with a standard deviation of 0.8 nm across the five data sets, while the RMS variation across the image was 6 nm with a 0.05 nm standard deviation across the five data sets. These measurements are consistent with the values expected from the $\lambda/10$ optics used in the interferometer, and show a high degree of repeatability.

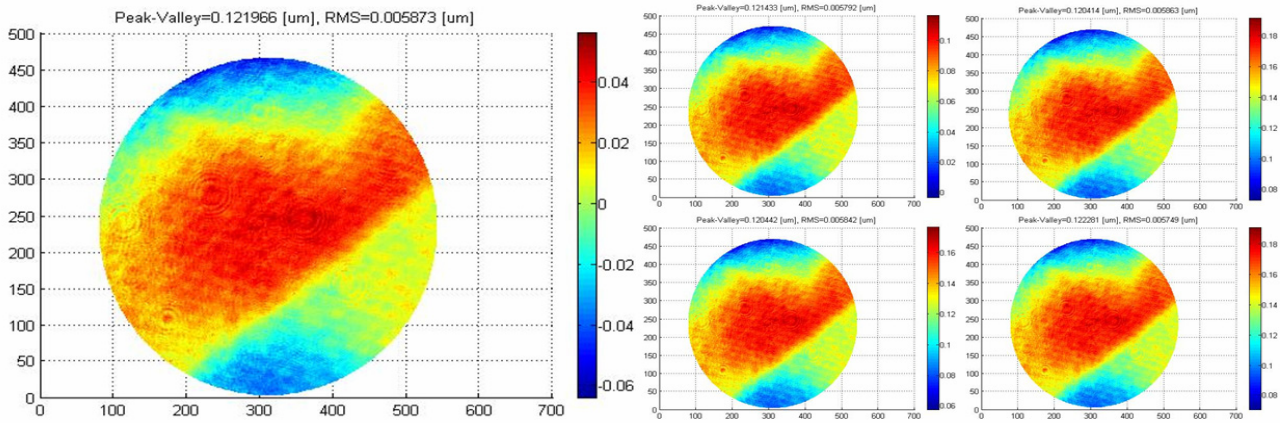

Figure 3: Surface height measurements obtained from 5 sequential measurements of a flat reference mirror.

3. MEASUREMENTS OF THE BIMORPH DEFORMABLE MIRROR

3.1. Static Measurements

Preliminary measurements of the nominally flat DM surface were obtained with the front face and all back face electrodes set to 100V. The resulting surface height map, illustrated in Figure 4, shows a variation of 600 nm peak-to-valley and 120 nm RMS. To isolate the effects of low spatial frequency variations which could theoretically be removed in a closed-loop AO system from the high spatial frequency surface roughness of the mirror, the data were fit using a 5th-order Zernike approximation. The residual error after this fit is illustrated in the figure and shows that a variation of 200 nm peak-to-valley and 13 nm RMS remains. The primary source of this residual surface roughness is small pits with a depth of approximately 150 nm and a diameter of 100-200 μm. These pits are attributed to defects in the surface produced when the ceramic surface of the DM is polished during manufacturing.

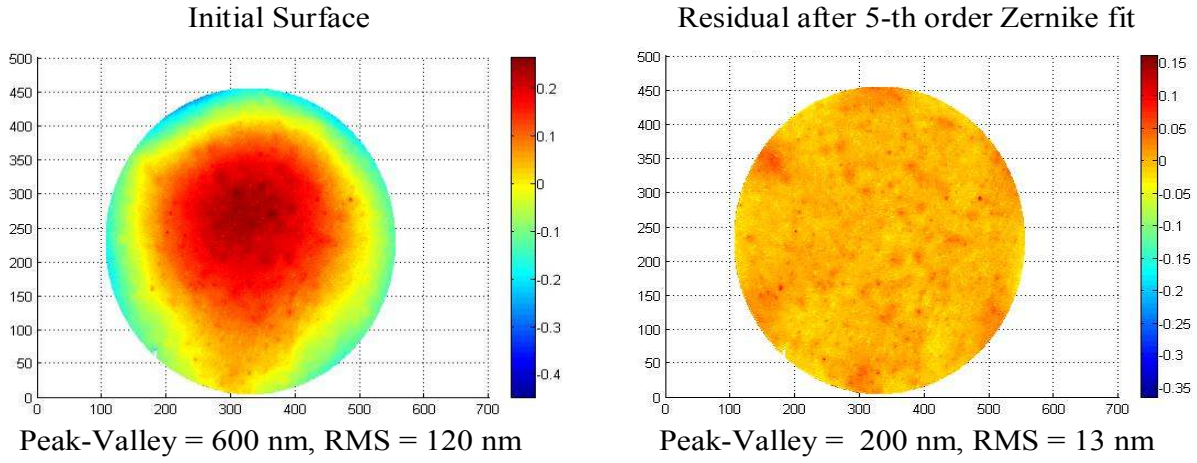

Figure 4: Measurements of flat DM. Left: measured mirror surface. Right: the residual error after a 5th order Zernike fit to the measured surface.

Maximum Stroke: Although the front face electrode is nominally biased at 100V and the back face electrodes are used to control the DM shape, the maximum parabolic deformation is obtained when the electric field-induced stress in either the top or bottom ceramic layer is minimized (by setting the potential across this layer to 0V) while the stress in the other layer is maximized (by setting the potential to 300V). This fact was utilized to characterize the maximum stroke available for defocus. The maximum convex deformation, measured at 20.8 μm, is produced when the front face electrode is driven to 300V while all back face electrodes (channels 1-35 and the guard ring) are grounded. Similarly, the maximum concave deformation, measured at 19.3 μm, is produced when the front face electrode is grounded while

all back face electrodes are driven to 300V. These parabolic deformations correspond to defocus values of –3.2 Diopters and +3.0 Diopters when measured across the 10.2 mm pupil.

Linearity: The linearity and hysteresis of the actuator characteristics were measured by holding the front face and guard ring electrodes at the nominal 100V bias voltage and driving all the back face electrodes from 0V to 300V and back again. The results of this test are shown in Figure 5. At voltages below approximately 50V, the mirror deformation displays a quadratic dependence on the applied voltage. Voltages from 50V to 200V result in a nearly linear displacement characteristic, and the polarization of the ceramic begins to saturate above 200V, with very little displacement occurring for voltages above 250V (E ≈ 1500 V/mm). The actuator hysteresis was measured to be 0.3 μm, approximately 2% of the full-scale peak-to-peak displacement of 16 μm.

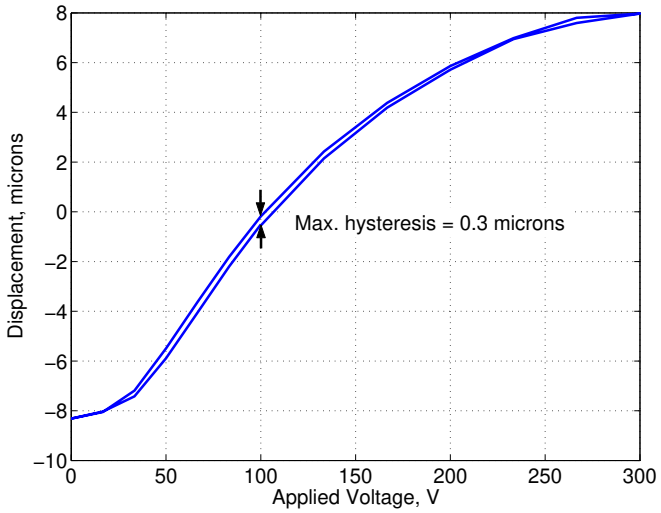

Figure 5: Measurement of actuator linearity and hysteresis. The front face and guard ring electrodes are held at 100V while all the remaining back face electrodes (channels 1-35) are driven from 0V to 300V.

3.2. Dynamic Measurements

The response of the DM to a step voltage input was measured using a Laser Doppler Vibrometer (Polytec OFV 3001). The results of this test are displayed in Figure 6. The initial step response, plotted in Figure 6(a), displays the characteristic ring-down of an under-damped second-order system with a natural frequency of f_n = 2.67 kHz and a quality factor of Q = 18, settling within 1% of the final position after approximately 10 ms. After this linear settling behavior, the DM displays a slow creep behavior, plotted in Figure 6(b), as the mirror position drifts by approximately 1% of the full-scale displacement over the next 60 ms. This creep behavior is commonly encountered in piezoelectric and electrostrictive actuators and has been noted in earlier publications on DM's constructed from PMN [18].

4. OPEN-LOOP GENERATION OF ZERNIKE MODES

Previous authors have noted that the stroke of a bimorph DM diminishes with the spatial frequency of the applied deformation. The relationship between stroke (Δz) and spatial frequency, k, is approximately described by [35]:

$$(1) \quad \Delta z \propto 1/k^2$$

This characteristic makes the bimorph DM well-suited to correct for astronomical turbulence, which diminishes in approximately the same fashion with spatial frequency.

To characterize the dependence of the DM stroke on the spatial frequency of deformation, a simple open-loop control method was developed. In this approach, the deformation of the DM surface is modeled as a weighted combination of the deformations contributed by each actuator channel, known as the actuator influence function. The deformation of the DM surface, $w(x, y)$, is described by:

$$(2) \quad w(x,y) = \sum_{i=1}^{N} f(v_i)\varphi_i(x,y)$$

where N represents the number of actuators on the DM, $\varphi_i(x, y)$ is the influence function and v_i is the control voltage applied to the i-th actuator, while $f(\ )$ represents the normalized actuator displacement as a function of applied voltage.

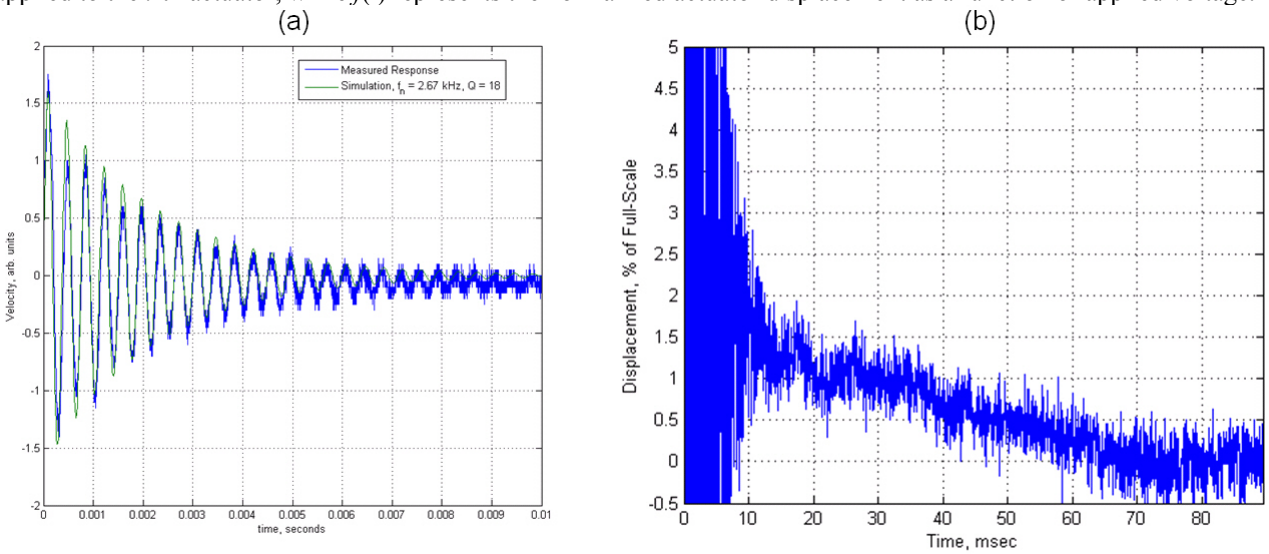

Figure 6: Step response measurements. The initial response is accurately described by an under-damped second order model with f_n = 2.67 kHz and Q = 18 (a). Following the initial 10 ms transient response, the DM displays a slow creep of 1% of full-scale displacement over the next 60 ms (b).

Note that in the case that the actuator displacement varies linearly with applied voltage, $f(v_i)$ is replaced by (v_i / v_{max}) in Eqn. (2). In vector-matrix form, Eqn. (2) becomes:

$$(3)\quad w(x,y) = f(\vec{v})\vec{\varphi}(x,y)^T$$

where $\vec{\varphi}(x,y) = [\varphi_1(x,y), \varphi_2(x,y), \cdots \varphi_N(x,y)]$ and $\vec{v} = [v_1, v_2, \cdots v_N]$.

The influence function for each of the $N = 35$ back face electrodes was measured by applying 300V to the desired channel and interferometrically measuring the resulting DM surface shape. The guard ring was not utilized in these tests and was held at a constant 100V potential equal to that of the front face electrode. The voltage to displacement characteristic, $f(\ )$, was approximated using the measurement of the DM stroke versus voltage shown in Figure 5.

Each measured influence function was then approximated with an M-dimensional combination of Zernike polynomials through a least-squares fit [34],[36]:

$$(4)\quad \varphi_i(x,y) = \sum_{j=1}^{M} a_{ij} z_j(x,y)$$

Where $z_j(x,y)$ is the j-th Zernike polynomial, and the a_{ij}'s are the coefficients used to fit the i-th influence function. Piston, the 0th order polynomial, was discarded after the least-squares fit. Expressed in vector-matrix form,

$$(5)\quad \vec{\varphi}(x,y)^T = A\vec{z}(x,y)^T$$

where $\vec{z}(x,y) = [z_1(x,y), z_2(x,y), \cdots z_M(x,y)]$ is the $1 \times M$ vector of Zernike polynomials and A is the $N \times M$ influence matrix. The present work explores using the DM to generate Zernike mode shapes up to the 5th radial order, so the maximum fit length was $M = 20$, resulting in a 35×20 A matrix. When A is decomposed using the singular-value decomposition, the magnitude of each singular value provides an indication of the DM's ability to reproduce each Zernike mode – singular values near zero indicate modes which are not controllable with the DM. The SVD is used to compute A^*, the pseudo-inverse of A, which in turn is used to calculate the vector of control voltages, $\vec{v}$, required to reproduce the desired combination of Zernike mode shapes. If the $1 \times M$ vector $\vec{e}$ represents the desired combination of Zernike modes, the required control voltages can be calculated from:

$$(6)\quad \vec{v} = f^{-1}(\vec{e}A^*)$$

In the case where the actuator displacement varies linearly with applied voltage, Eqn. (6) becomes:

$$(7) \quad \vec{v} = v_{\max} \vec{e} A^*$$

Since $f()$ is not generally invertible, the function is approximated using a third-order polynomial fit of the measured voltage to displacement curve and the inversion is performed using a look-up table which maps actuator displacement to control voltages. Eqn. (6) was used to calculate the control voltages required to generate each Zernike mode shape up to 5th order. To determine the maximum Peak-to-Valley displacement achievable for each mode, the amplitude of each mode was progressively increased in the input vector $\vec{e}$ until the computed control voltage on any one actuator channel exceeded the maximum limits available from the high-voltage amplifier. Since one may suppress uncontrollable modes by eliminating modes corresponding to relatively small singular values in the SVD, the algorithm offers some flexibility to reduce errors which might be contributed by these modes.

The open-loop approach has the following limitations. First, the model proposed in Eq (2) does not account for any initial deformation in the mirror surface when the control voltages are set to zero. As a result, any initial deformation in the mirror surface will be present in all replicated surfaces. Since our objective was to make a coarse measurement of the actuator stroke in each mode, rather than to perform precise open-loop replication of particular mode shapes, we did not seek to eliminate this initial deformation through a more complicated control algorithm. Second, since the control voltages are computed in one step, rather than iteratively as in a true closed-loop AO system, any small numerical errors can cause the calculated voltage required of a single actuator channel to saturate prematurely, limiting the maximum stroke attained for a particular mode. In a closed-loop AO system, the saturation of a single actuator channel does not halt the adaptive control routine since the wavefront error is not minimized at this point (it is an iterative process which converges to the solution). Our data show evidence that this saturation effect is a problem in some modes, but the simplicity of the open-loop approach does allow for quick characterization of actuator stroke at each spatial frequency.

The results of the open-loop mode shape generation tests are summarized in Table 2 and Figure 7. Three important results are evident in the data. First, the actuator saturation effect described above was a problem for the Defocus (Z_2^0) and 90º Astigmatism modes (Z_2^{+2}). In the earlier test used to characterize actuator stroke, where all back face electrodes were driven with a common voltage, a parabolic deformation of approximately ±8 μm was generated. This earlier result is consistent with the 7.5 μm amplitude achieved for the 45º Astigmatism mode (Z_2^{-2}), so it is expected that this represents the true amplitude achievable for 2nd order aberrations. Second, the maximum mode shape amplitude is approximately proportional to the inverse square of the mode's radial order, e.g. the amplitude for 2nd order modes is approximately 8 μm, for 3rd order modes it diminishes by about $(2/3)^2$ to 3.5 μm, for 4th order it falls by $(2/4)^2$ to 2 μm, and for 5th order modes it drops by $(2/5)^2$ to 1.3 μm. Third, the RMS error for each mode shape is approximately constant for all mode shapes, and is nearly equal to the RMS error present in the flat mirror surface. While the RMS error for most of the mode shapes appears to be distributed somewhat randomly over a variety of spatial frequencies, the four 3rd order modes show distinctive coupling to their 5th order counterparts. This fact is illustrated in Figure 8, which shows the RMS error for these four modes (Trefoil 1, Horizontal Coma, Vertical Coma, and Trefoil 2) decomposed using the first 20 Zernike coefficients. In the figure, the Zernike polynomials are numbered sequentially, using the single-index notation from Malacara [34]. The figure shows that the RMS error for each 3rd order mode is mainly due to a strong component of the corresponding 5th order mode (i.e. the RMS error of Trefoil 1, Z_3^{-3}, is mainly contributed by Z_5^{-3}). No similar coupling was observed between 2nd and 4th order modes, where the RMS errors were distributed roughly randomly between the various Zernike modes.

5. DISCUSSION AND CONCLUSIONS

Porter, et al. [37] studied the impact of high order aberrations on the vision of a large group of subjects with normal vision (109 subjects; age range between 20 to 70 years old; age average around 40 years old): defocus and astigmatism represent 92% of the total wavefront aberrations. In general, the aberration magnitude diminishes with increasing radial order. The dominant higher order aberrations are coma (Z_3^{-2} and Z_3^{+2}) and spherical aberration (Z_4^0), which account for 1.8% and 1.6 % of the total RMS wavefront error, respectively. The effect of higher order aberrations on human vision quality increases with the pupil size. For a small pupil size (3 mm), the RMS wavefront error contributed by aberrations above the 3rd order is extremely small and these aberrations do not contribute significantly to the degradation of the image quality of a normal eye [12]. In this case, the AOptix DM, with its capability to reconstruct Zernike modes up to

the 5th order, appears to be a good potential wavefront corrector for vision science purposes. At larger pupil sizes (7.3 mm), the Zernike modes up to the 8th order make a significant contribution to image quality. In this case, a potential solution would be to cascade the AOptix DM with a second DM with a greater number of actuators, such as the Boston Micromachines DM. In such a system, the bimorph would be used to correct for the large amplitude, low order aberrations, while the high order aberrations would be corrected with the second DM.

As expected for a bimorph DM, the AOptix device is capable of generating large displacements at low spatial frequencies. At a constant front-face voltage of 100V, the measured peak-to-valley surface displacement was approximately ±8 μm for the 2nd order aberrations of defocus and astigmatism, corresponding to a defocus of ±1.2 Diopters over the 10.2 mm DM pupil. For comparison, this is four times the range of defocus and eight times the range of astigmatism recently reported by Fernandez for the OKO Technologies MEMS DM [20]. In addition, by varying the potential of the front-face electrode, the AOptix device can generate an even larger range of ±3 Diopters of defocus. Although the maximum deformation that the DM can generate diminishes approximately with the square of the mode's radial order, we were able to generate 5th order modes with 1 μm to 1.5 μm of peak-to-valley deformation. Because this range of deformations is comparable to that expected from the 2 μm stroke Boston Micromachines DM, it is expected that both DM's will display similar capabilities for correcting aberrations up to the 5th radial order. Moreover, we have not yet explored how the amplitude of each mode is limited when the mirror is used to generate a combination of multiple modes simultaneously. Our future work will focus on integrating the AOptix DM into a closed-loop AO system and measuring the ability of the DM to correct for these aberrations.

Table 2: Summary of maximum peak-to-valley deformation and RMS error for generated Zernike modes.

Radial Order	Angular Frequency	Description	Peak-Valley [um]	RMS error [um]
2	-2	Astigmatism (-45 & +45)	7.464	0.164
	0	Defocus	3.232*	0.264
	+2	Astigmatism (0 & 90)	6.078*	0.304
3	-3	Trefoil 1	4.205	0.151
	-1	Vertical Coma	2.510	0.139
	+1	Horizontal Coma	2.186	0.156
	+3	Trefoil 2	3.357	0.153
4	-4	Quadrafoil 1	2.749	0.156
	-2	Secondary astigmatism 1	1.718	0.121
	0	Spherical Aberration	1.295	0.125
	+2	Secondary astigmatism 2	1.578	0.090
	+4	Quadrafoil 2	2.279	0.143
5	-5	Pentafoil 1	1.511	0.166
	-3	Secondary Trefoil 1	1.161	0.110
	-1	Secondary Coma 1	1.399	0.114
	+1	Secondary Coma 2	1.063	0.110
	+3	Secondary Trefoil 2	1.480	0.143
	+5	Pentafoil 2	1.474	0.143

* Limited by saturation of a single actuator. The actual limit is expected to be approximately 8μm.

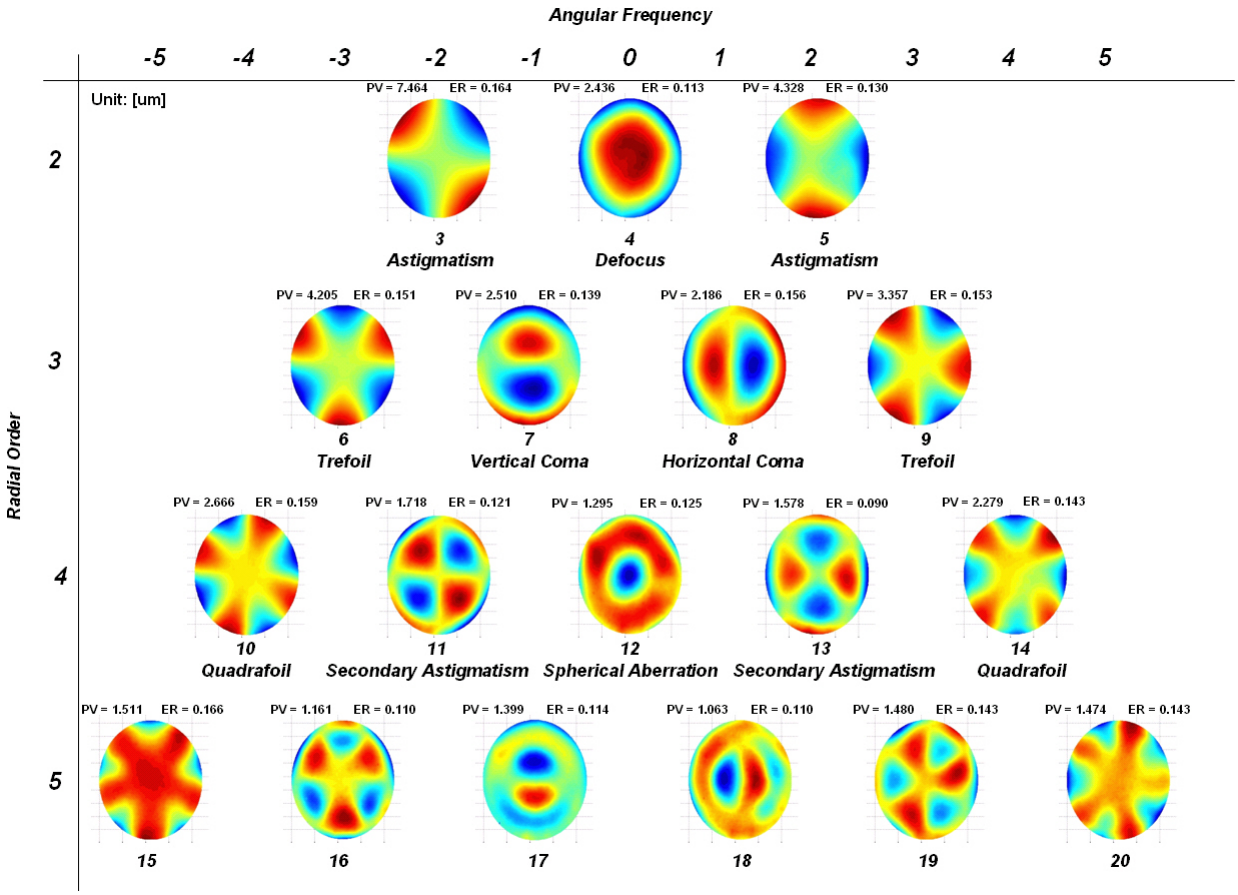

Figure 7: Replication of Zernike mode shapes using the open-loop control method.

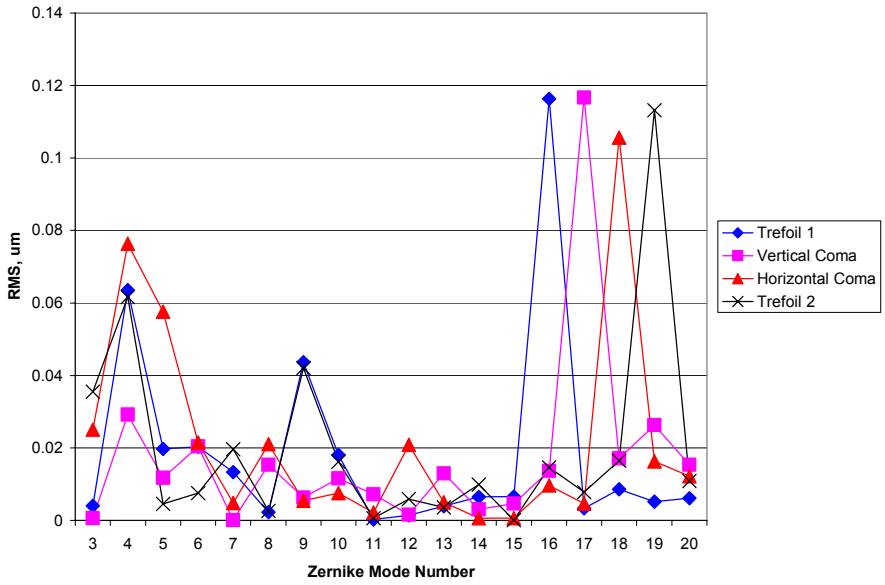

Figure 8: RMS error resulting from the replication of the four 3rd order Zernike modes. In each case, the RMS error is predominantly contained in the corresponding 5th order mode.

ACKNOWLEDGEMENTS

The authors acknowledge the help of J. Elon Graves from AOptix Technologies for providing the deformable mirror and for his useful comments, Steve Jones from Lawrence Livermore National Laboratory for his technical advice, and Angela Haff for her help in the characterization of the device. Supported by the National Eye Institute (grant EY 014743).

David Horsley is an Assistant Professor in the Department of Mechanical and Aeronautical Engineering at the University of California, Davis. He received the Ph.D. degree in Mechanical Engineering from the University of California at Berkeley in 1998. His interests include micro-electromechanical systems (MEMS), sensors, and control systems.

Sophie Laut is a postdoctoral researcher at the Department of Ophthalmology and Visual Science at the University of California, Davis. She holds a M. Engineering degree in Computer Science and Industrial Control System, and a Ph.D. degree in Electrical and Computer Engineering, specialization in optical processing, in 2000 from the Université de Haute-Alsace, Mulhouse (France). Her interests include adaptive optics, wave front sensors and correctors, optical information processing and diffractive optics.

REFERENCES

[1] D. Miller, "Retinal Imaging and Vision at the Frontiers of Adaptive optics," in *Physics Today*, 2000, pp. 31-36.

[2] J. Liang, D. Williams, and D. Miller, "Supernormal vision and high-resolution retinal imaging through adaptive optics," *JOSA A*, vol. 14, pp. 2884-2892, 1997.

[3] M. Glanc, E. Gendron, F. Lacombe, D. Lafaille, J.-F. Le Gargasson, and P. Lena, "Towards wide-field retinal imaging with adaptive optics," *Optics Communications*, vol. 230, pp. 225-238, 2003.

[4] A. Larichev, P. Ivanov, N. Iroshnikov, V. Shmalhauzen, and L. Otten, "Adaptive system for eye-fundus imaging," *Quantum Electronics (Kvantovaya Elektronika)*, vol. 32, pp. 902-908, 2002.

[5] G. Erry, L. Otten, A. Larichev, and N. Irochnikov, "A High Resolution Adaptive Optics Fundus Imager," presented at 4th International Workshop on Adaptive Optics for Industry and Medicine, Muenster, Germany, 2003.

[6] N. Doble, G. Yoon, L. Chen, P. Bierden, B. Singer, S. Olivier, and D. Williams, "Use of a microelectromechanical mirror for adaptive optics in the human eye," *Optics Letters*, vol. 27, pp. 1537-1539, 2002.

[7] H. Hofer, L. Chen, G. Yoon, B. Singer, Y. Yamauchi, and D. Williams, "Improvement in retinal image quality with dynamic correction of the eye's aberrations," *Optics Express*, vol. 8, pp. 631-643, 2001.

[8] N. Ling, Y. Zhang, X. Rao, X. Li, C. Wang, Y. Hu, and W. Jiang, "Small table-top adaptive optical systems for human retinal imaging," presented at High-Resolution Wavefront Control: Methods, Devices, and Applications IV, 2002.

[9] A. Roorda, F. Romero-Borja, W. Donnelly III, and H. Qneener, "Adaptive optics scanning laser ophthalmoscopy," *Optics Express*, vol. 10, pp. 405-412, 2002.

[10] B. Vohnsen, I. Iglesias, and P. Artal, "Confocal scanning laser ophthalmoscope with adaptive optical wavefront correction," presented at Three-Dimensional Microscopy: Image Acquisition and Processing X, 2003.

[11] B. Hermann, E. Fernandez, A. Unterhuber, H. Sattmann, A. Fercher, W. Drexler, P. Priesto, and P. Artal, "Adaptive-optics ultrahigh-resolution optical coherence tomography," *Optics Letters*, vol. 29, pp. 2142-2144, 2004.

[12] J. Liang and D. Williams, "Aberrations and Retinal image quality of the normal human eye," *JOSA A*, vol. 14, pp. 2873-2883, 1997.

[13] D. Williams, G.-Y. Yoon, J. Porter, A. Guirao, H. Hofer, and I. Cox, "Visual Benefits of Correcting Higher Order Aberrations of the Eye," *Journal of Refractive Surgery*, vol. 16, pp. S554-, 2000.

[14] X. Cheng, A. Bradley, L. Thibos, and S. Ravikumar, "Visual impact of monochromatic aberrations," *Invest Ophthalmolo Vis Sci*, vol. E-Abstract 2123, 2003.

[15] N. Doble and D. Williams, "The Application of MEMS Technology for Adaptive Optics in Vision Science," *Journal of Selected Topics in Quantum Electronics*, vol. 10, pp. 629-635, 2004.
[16] G. Love, "Liquid crystal adaptive optics," in *Adaptive optics engineering Handbook*, R. Tyson, Ed.: Marcel Dekker, 2000, pp. 273-285.
[17] F. Vargas-Martin, P. Prieto, and P. Artal, "Correction of the aberrations in the human eye with a Liquid-Crystal Spatial Light Modulator: limits to performance," *JOSA A*, vol. 15, pp. 2552-2562, 1998.
[18] B. R. Oppenheimer, D. Palmer, R. Dekany, A. Sivaramakrishnan, M. Ealey, and T. Price, "Investigating a Xinetics Inc. Deformable Mirror," presented at Proceedings of the SPIE, Vol. 3126, 1997.
[19] A. Awwal, B. Bauman, D. Gavel, S. Olivier, S. Jones, D. Silva, J. Hardy, T. Barnes, and J. Werner, "Characterization and Operation of a Liquid Crystal Adaptive Optics Phoropter," presented at Astronomical Adaptive Optics Systems and Applications, 2003.
[20] E. Fernandez and P. Artal, "Membrane deformable mirror for adaptive optics: performance limits in visual optics," *Optics Express*, vol. 11, pp. 1056-1069, 2003.
[21] L. Zhu, P.-C. Sun, D.-U. Bartsch, and W. Freeman, "Wave-front generation of Zernike polynomial modes with a micromachined membrane deformable mirror," *Applied Optics*, vol. 38, pp. 6019-6026, 1999.
[22] N. Doble, G. Yoon, L. Chen, P. Bierden, B. Singer, S. Olivier, and D. R. Williams, "Use of a microelectromechanical mirror for adaptive optics in the human eye," *Optics Letters*, vol. 27, pp. 1537-1539, 2002.
[23] G. Vdovin and P. M. Sarro, "Flexible mirror micromachined in silicon," *Applied Optics*, vol. 34, pp. 2968-2972, 1995.
[24] T. Bifano, J. Perrault, R. Mali, and M. Hernstein, "Microelectromechanical Deformable Mirrors," *IEEE Journal of Selected Topics in Quantum Electronics*, vol. 5, pp. 83-89, 1999.
[25] J. Graves, M. Northcott, F. Roddier, C. Roddier, D. Potter, D. O'Connor, F. Rigaut, and M. Chun, "First light for Hokupa'a 36 on Gemini North," presented at Adaptive optical System Technologies, 2000.
[26] G. H. Haertling, "Ferroelectric ceramics: history and technology," *Journal of the American Ceramic Society*, vol. 82, pp. 797-818, 1999.
[27] G. H. Blackwood and M. A. Ealey, "Electrostrictive behavior in lead magnesium niobate (PMN) actuators. Part 1: Materials perspective.," *Smart Materials & Structures*, vol. 2, pp. 124-133, 1993.
[28] C. L. Hom, P. D. Dean, and S. R. Winzer, "Modeling electrostrictive deformable mirrors in adaptive optics systems," presented at Smart Structures and Materials 2000: Smart Structures and Integrated Systems, 2000.
[29] C. Schwartz, E. Ribak, and S. G. Lipson, "Bimorph adaptive mirrors and curvature sensing," *J. Opt. Soc. Am. A*, vol. 11, pp. 895-902, 1994.
[30] E. M. Ellis, "Low-cost bimorph mirrors in adaptive optics," in *Department of Physics*. London: Imperial College of Science Technology and Medicine, 1999.
[31] M. R. Hart, R. A. Conant, K. Y. Lau, and R. S. Muller, "Stroboscopic interferometer system for dynamic MEMS characterization," *Journal of Microelectromechanical Systems*, vol. 9, pp. 409-418, 2000.
[32] C. Rembe and R. S. Muller, "Measurement system for full three-dimensional motion characterization of MEMS," *Journal of Microelectromechanical Systems*, vol. 11, pp. 479-488, 2002.
[33] P. Hariharan, B. F. Oreb, and T. Eiju, "Digital Phase-Shifting Interferometry - a Simple Error-Compensating Phase Calculation Algorithm," *Applied Optics*, vol. 26, pp. 2504-2506, 1987.
[34] D. Malacara, *Optical Shop Testing*: John Wiley & Sons, 1992.
[35] F. Roddier, *Adaptive optics in astronomy*. New York: Cambridge University Press, 1999.
[36] J. Y. Wang and D. E. Silva, "Wave-Front Interpretation with Zernike Polynomials," *Applied Optics*, vol. 19, pp. 1510-1518, 1980.
[37] J. Porter, A. Guirao, I. Cox, and D. Williams, "Monochromatic aberrations of the human eye in a large population," *JOSA A*, vol. 18, pp. 497-506, 2001.